

# Self-powered sensing platform based on triboelectric nanogenerators towards intelligent mining industry

Received: 28 November 2024

Accepted: 22 May 2025

Published online: 03 June 2025

 Check for updates

Lindong Liu<sup>1,2,6</sup>, Yurui Shang<sup>2,3,6</sup>, Andy Berbille<sup>2,3,6</sup>, Morten Willatzen<sup>2,3,4</sup>, Yuan Wang<sup>1</sup>✉, Xunjia Li<sup>2</sup>, Longyi Li<sup>2,3</sup>, Xiongxin Luo<sup>2,3</sup>, Jianwu Chen<sup>1,5</sup>, Bin Yang<sup>1,5</sup>, Cuifeng Du<sup>1</sup>✉, Zhong Lin Wang<sup>2,3</sup>✉ & Laipan Zhu<sup>2,3</sup>✉

Gold's crucial role in economic and technological developments has driven the industry towards underground mining, with air quality concerns challenging workers' safety. Currently, commercial solutions to assess air quality and safety in underground mines often suffer from low accuracy, high installation and maintenance costs, without providing data on noxious gases. To address these limitations, we developed a triboelectric self-powered sensing-platform (TESS) employing two distinct triboelectric nanogenerators (TENGs) modules to achieve power generation and wind-speed sensing function, with an ultra-low starting wind speed ( $0.32 \text{ m s}^{-1}$ ), capable of operating for up to 3 months in underground mining tunnels. Wind-sensing capabilities are accrued by a horizontal turbine based on non-contact TENGs. Meanwhile, the TESS is powered by a distinct array of TENGs that operates via a new working mode, balancing the advantages of contact-separation and free-standing modes. Assisted by an optimized self-driven power management system, the TESS attains a charging power density of  $16.36 \text{ mW m}^{-2}$ ; this power is delivered every 166 s to a sensor node (temperature, relative humidity, pressure, and concentrations of CO, NO<sub>2</sub>, NH<sub>3</sub>), a data processing unit, and a LoRa transmitter. This work represents a leap forward in developing robust, cost-effective, battery-free, and wireless TENG-based environmental sensing platforms.

Gold plays a central role in modern economies, serving as a financial asset and a critical material in various industries, including electronics manufacturing<sup>1–3</sup>, medicine<sup>4–6</sup>, catalysis<sup>7,8</sup>, and even space exploration<sup>9</sup>. Nowadays, gold is mainly extracted from underground mining sites, where workers face multiple safety and health hazards, including temperatures above 308.15 K, relative humidity exceeding 90%, and noxious gases released by explosions and exhaust from heavy machinery<sup>10–13</sup>. To mitigate these risks, extensive ventilation systems

are employed to intake fresh air, dilute pollutants, and expel noxious gases<sup>10,14</sup>. However, these large and complex systems (Supplementary Fig. 1) are prone to malfunction, making continuous monitoring through a dense array of wind-speed sensors crucial for maintaining safe operational conditions<sup>15</sup>.

The use of commercially available wind-speed sensors (such as differential pressure, ultrasonic and mechanical types, Supplementary Note 1) commonly employed in mining environments presents several

<sup>1</sup>School of Civil and Resource Engineering, University of Science and Technology Beijing, Beijing, P.R. China. <sup>2</sup>Beijing Key Laboratory of Micro-nano Energy and Sensor, Center for High-Entropy Energy and Systems, Beijing Institute of Nanoenergy and Nanosystems, Chinese Academy of Sciences, Beijing, P.R. China. <sup>3</sup>School of Nanoscience and Engineering, University of Chinese Academy of Sciences, Beijing, P.R. China. <sup>4</sup>Department of Mathematical Sciences, Aalborg University, Aalborg, DK, Denmark. <sup>5</sup>China Academy of Safety Science and Technology, Beijing, P.R. China. <sup>6</sup>These authors contributed equally: Lindong Liu, Yurui Shang, Andy Berbille. ✉ e-mail: [yuanwang@ustb.edu.cn](mailto:yuanwang@ustb.edu.cn); [ducuifeng@ces.ustb.edu.cn](mailto:ducuifeng@ces.ustb.edu.cn); [zhong.wang@mse.gatech.edu](mailto:zhong.wang@mse.gatech.edu); [zhulaipan@binn.cas.cn](mailto:zhulaipan@binn.cas.cn)

notable challenges. (1) Extensive tunnel construction is typically required before installing these sensors, preventing their operation at the initial stages of tunnel construction. (2) These sensors rely on photoelectric, electromagnetic, or ultrasonic converters that require a continuous source of power to transform wind speed into electrical signals. (3) The data and power cables they rely on are often vulnerable to damage caused by geological events and vehicles (see Supplementary Fig. 2). (4) These sensors tend to accumulate contaminants within 2 to 3 weeks including water seepage, debris and dust (Supplementary Fig. 3), necessitating frequent inspection and maintenance, and associated costs. (5) Finally, relying solely on ventilation system wind-speed measurements as a proxy for air quality is inadequate. Indeed, the measurement of hazardous gases concentrations is often overlooked, posing serious safety risks. Serious poisoning events highlight the critical need for direct monitoring of noxious gases alongside ventilation parameters<sup>16,17</sup>. To facilitate widespread adoption, monitoring systems should be cost-effective, power-efficient, battery-free, and wireless, while providing real-time data on wind speed, concentrations of common noxious gases, and other environmental parameters, such as temperature, relative humidity (RH), air pressure.

Here, to address the aforementioned challenges, we designed a self-powered wireless sensing-platform based on triboelectric nanogenerators (TENGs) for wind-speed sensing and power generation, named TESS (triboelectric self-powered sensing-platform). TENGs are devices capable of converting high entropy mechanical energy from the environment into electricity by coupling the triboelectric charging of dielectric materials with electrostatic induction in metal electrodes<sup>18–20</sup>. The wind-sensing functionality is achieved through a self-powered, non-contact TENG actuated by a curved-edge turbine, which provides excellent linearity and operates with a starting wind speed as low as  $0.32 \text{ m s}^{-1}$ . Furthermore, the TESS is equipped with low-power sensors to monitor temperature, RH, air pressure, and the concentrations of CO, NO<sub>2</sub>, and NH<sub>3</sub>. Meanwhile, it is capable of measuring, processing and transmitting these data to a handheld device twice for every working cycle of 166 s. To ensure stable power output to the load circuit, the TESS employs a Mixed-Mode TENG, combining the advantages of free-standing and contact-separation TENGs, paired with an optimized self-driven power management system. This system charges an energy-storage capacitor with a charging power density (call power density, Supplementary Note 2) of  $16.36 \text{ mW m}^{-2}$  under a wind speed of  $4.05 \text{ m s}^{-1}$ . Notably, the TESS has a compact design with dimensions of only  $190 \times 190 \times 200 \text{ mm}^3$ . Field test conducted in an actual gold mine demonstrated that, under average conditions of  $4.25 \text{ m s}^{-1}$  wind speed and 91.2% RH, the TESS power supply system could operate continuously for over three months without any maintenance requirements. Given the advantages of TESS in enabling simultaneous, real-time monitoring of multiple parameters, along with its battery-free, wireless, and low-maintenance characteristics, the TESS demonstrates great application potential in the field of environmental sensing.

## Results

### Overview on the application scenario, general structure of the TESS, and overall performances

To provide clearer picture of the application scenario discussed in the introduction, Fig. 1a presents a simplified schematic of an underground mining site, showing the mining tunnels, airflow direction, and sources of hazardous gases (CO, NO<sub>2</sub>, NH<sub>3</sub>). In this application scenario, the TESS, designed with a compact footprint of  $190 \times 190 \times 200 \text{ mm}^3$  for convenient installation near the tunnel ceiling, serves as a replacement for traditional wind-speed sensors.

When the ventilation system operates, airflow passes through the tunnels, reaching the TESS. This airflow activates both the cylindrical non-contact TENG (serving as a self-powered wind-speed sensor) and

the Mixed-Mode TENGs (functioning as power generators) placed in a 3D-printed enclosure. As the four Mixed-Mode TENGs generate power, it is converted by a power management system (PMS) and then supplied to the CO, NO<sub>2</sub>, and NH<sub>3</sub> gas sensors, as well as sensors for temperature, RH, and air pressure. Additionally, a data acquisition module, powered also by the TENGs, aggregates and compiles the sensors' data, including wind speed from the non-contact TENG. The power output is sufficient to support an additional wireless transmission module, allowing real-time data to be relayed to either a control center or handheld devices, enabling miners to monitor environmental conditions locally before and during tunnel entry. The non-contact TENG-based wind-speed sensor is activated at a starting wind speed of just  $0.32 \text{ m s}^{-1}$ , a threshold lower than that of other turbine-based TENG wind-speed sensors, such as those utilizing blade or wind-cup turbines (Fig. 1b). After conversion, the Mixed-Mode TENGs achieve an ultra-high power density of  $16.36 \text{ mW m}^{-2}$  at a wind speed of  $4.05 \text{ m s}^{-1}$  (Supplementary Table 1 for comparison), which surpasses those of other single-end fixed TENGs (Fig. 1c). As demonstrated later in the manuscript, field tests indicate that the Mixed-Mode TENGs can continuously supply power to the circuit board for more than three months, highlighting the high durability of this TENG design (Fig. 1d). These features were achieved through a rigorous analysis of fluid dynamics' impact on the TENGs performance to optimize the structure, along with a systematic optimization of the dielectric film material properties and circuit design to enhance power management and efficiency.

### Self-powered wind-speed sensor with low starting wind speed: design, optimization, and calibration

Wind-speed monitoring is a critical parameter for evaluating the proper operation of ventilation systems in mining environments<sup>15</sup>. This study initially focuses on the development of a self-powered wind-speed sensor based on TENG technology. Considering that airflow within tunnel is predominantly unidirectional, with wind speeds ranging from 2 to  $6 \text{ m s}^{-1}$  (not exceeding  $10 \text{ m s}^{-1}$ ), our design targets include achieving high linearity within the range of  $1\text{--}9 \text{ m s}^{-1}$ , while ensuring a starting wind speed below  $0.8 \text{ m s}^{-1}$  (Supplementary Note 3). To meet these design requirements, we adopted a low-friction design that employs a turbine-based, non-contact TENG. This approach permits a more effective energy capture from unidirectional airflow than conventional vertical-axis turbines.

The structure of the non-contact TENG wind-speed sensor, illustrated in Fig. 2a, comprises two primary components: a three-dimensional (3D)-printed air duct featuring a concentric reducer and the non-contact TENG itself. The latter consists of two parts: (1) a 3D-printed curved-edge turbine equipped with winglets (indicated in blue) along the edges of the two blades (shown in yellow), on which a polytetrafluoroethylene (PTFE) film (acting as an electret) is affixed; and (2) four conformal spiraled copper (Cu) electrodes strategically positioned along the air duct, facing the blades' winglets and adopting the same curvature. The electrodes are paired, with opposing electrodes connected in sets of two to form two poles of opposite charge within the TENG. To prevent contact between the copper electrodes and PTFE films, a fixed distance of 2 mm is maintained between the turbine's winglets and the air duct. Detailed dimensions and fabrication processes are provided in the Methods section.

In Fig. 2b, we present a graphical description of the working principle of the non-contact TENG at the heart of the wind-speed sensor. The structure of the non-contact TENG is that of a free-standing TENG (Supplementary Fig. 4). The electret film placed on the winglet carries an electrostatic charge acquired during its detachment from the adhesive substrate and through friction with the air during turbine rotation<sup>21</sup> (Supplementary Note 4). At the initial position (Fig. 2b, la), the charged film remains stationary, spanning between

two electrodes of different pairs, resulting in a null open-circuit voltage. As airflow rushes in the air duct, the turbine starts rotating counterclockwise, leading the negatively charged PTFE film to face a pair of opposing electrodes after completing a  $\pi/4$  radians rotation (Fig. 2b, Ib). Due to electrostatic induction, the pair of opposing electrodes becomes positively charged while the other pair remains unpolarized. Consequently, the non-contact TENG generates a maximum positive voltage of +8.9 V. As the turbine continues its rotation to  $\pi/2$  radians, the voltage output decreases toward 0 V, since the electret films transition across electrodes of different pairs (Fig. 2b, Ic). Following this, as the turbine rotates towards its  $3\pi/4$  radians position, the voltage increases until reaching a maximum negative value of -8.9 V (Fig. 2b, Id). Upon completing its  $\pi$  radians rotation from the initial stage, the voltage reaches 0 V again, thereby finishing one full cycle of the signal. When the turbine completes a rotation of  $7/4\pi$  radians, the voltage reaches the maximum negative value of the

second cycle (Fig. 2b, II). After a complete rotation of  $2\pi$  radians, the device generates two signal periods. This working principle implies that, when analyzing the data for wind-speed evaluation, it is essential to focus on the frequency of the signal rather than the voltage output (Supplementary Note 5).

With this principle in mind, we investigated the influence of the turbine's structure on the starting wind speed. Specifically, we considered two parameters: the number of blades,  $n$ , and the angle  $\theta$  formed by the upstream and downstream edges of the blade when projected onto a plane, with  $n = 2, 3$ , or 4, and  $\theta = 90^\circ, 120^\circ$ , or  $180^\circ$ . We fabricated six different turbine designs (Supplementary Table 2). The experiment results, presented in Fig. 2d, indicated that the lowest starting wind speed,  $0.32 \text{ m s}^{-1}$ , was achieved with a turbine configuration of  $n = 2$  and  $\theta = 180^\circ$ . To elucidate why this particular combination of parameters leads to the lowest starting wind speed, we employed CFD (Computational Fluid Dynamics) analysis (Fig. 2e).

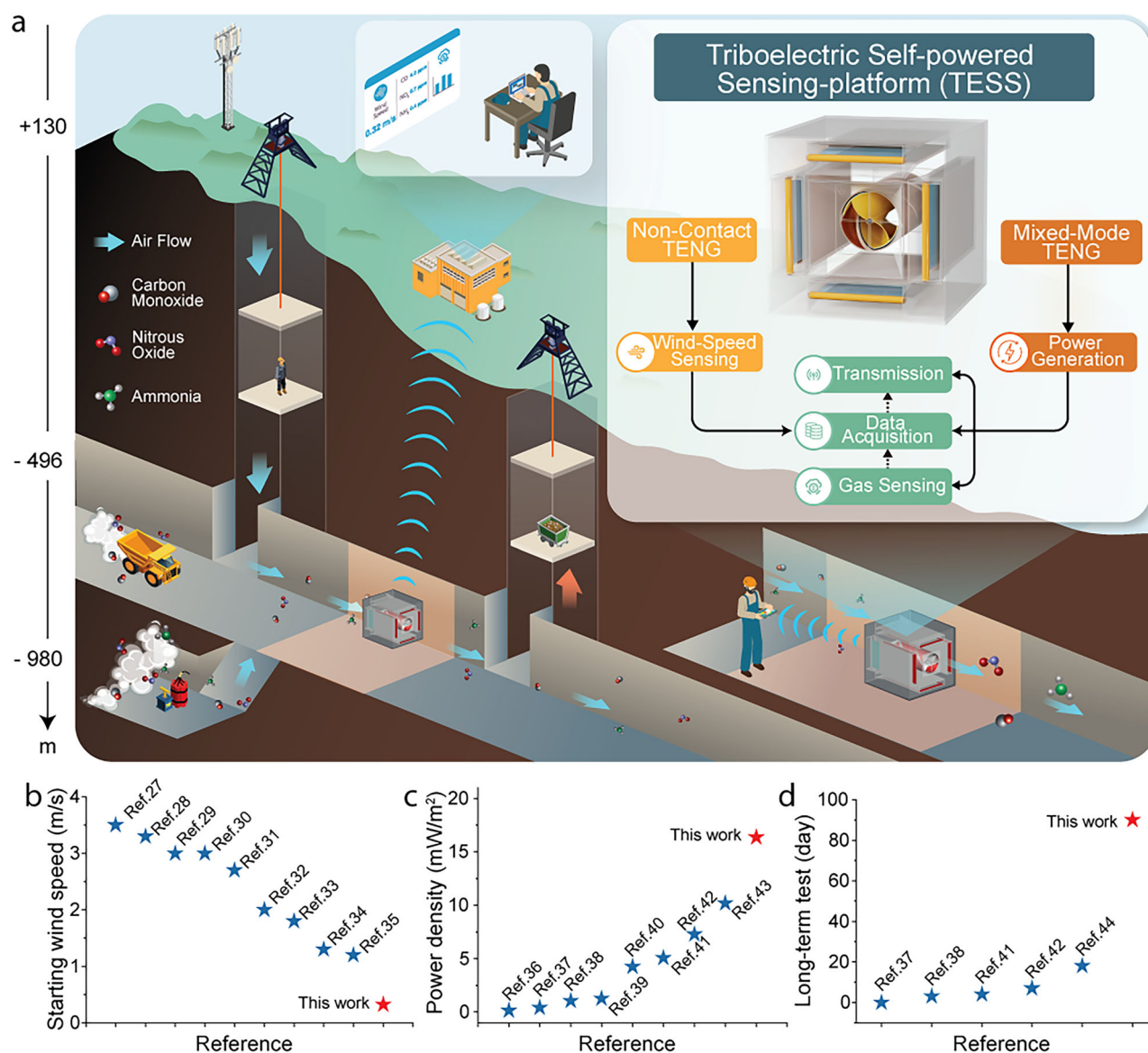


**Fig. 1 | Monitoring environmental parameters in mine with wind-driven triboelectric nanogenerators.** **a** A graphical overview illustrating the application of the TESS in an underground mine. The inset in the top-right corner presents a simplified outline of the TESS structure, showing its various modules and functions. **b** Comparison of starting wind speed between various turbine-based TENG wind-speed sensors reported in the literature (Ref. 27–35) and that incorporated in

the TESS. **c** Comparison of power density between single-end fixed TENGs from the literature (refs. 36–43) and the Mixed-Mode TENGs employed to power the TESS. **d** Durability performance comparison, expressed in days of constant operations, between TENGs from the literature (refs. 37, 38, 41, 42, 44) and that employed to power the TESS.

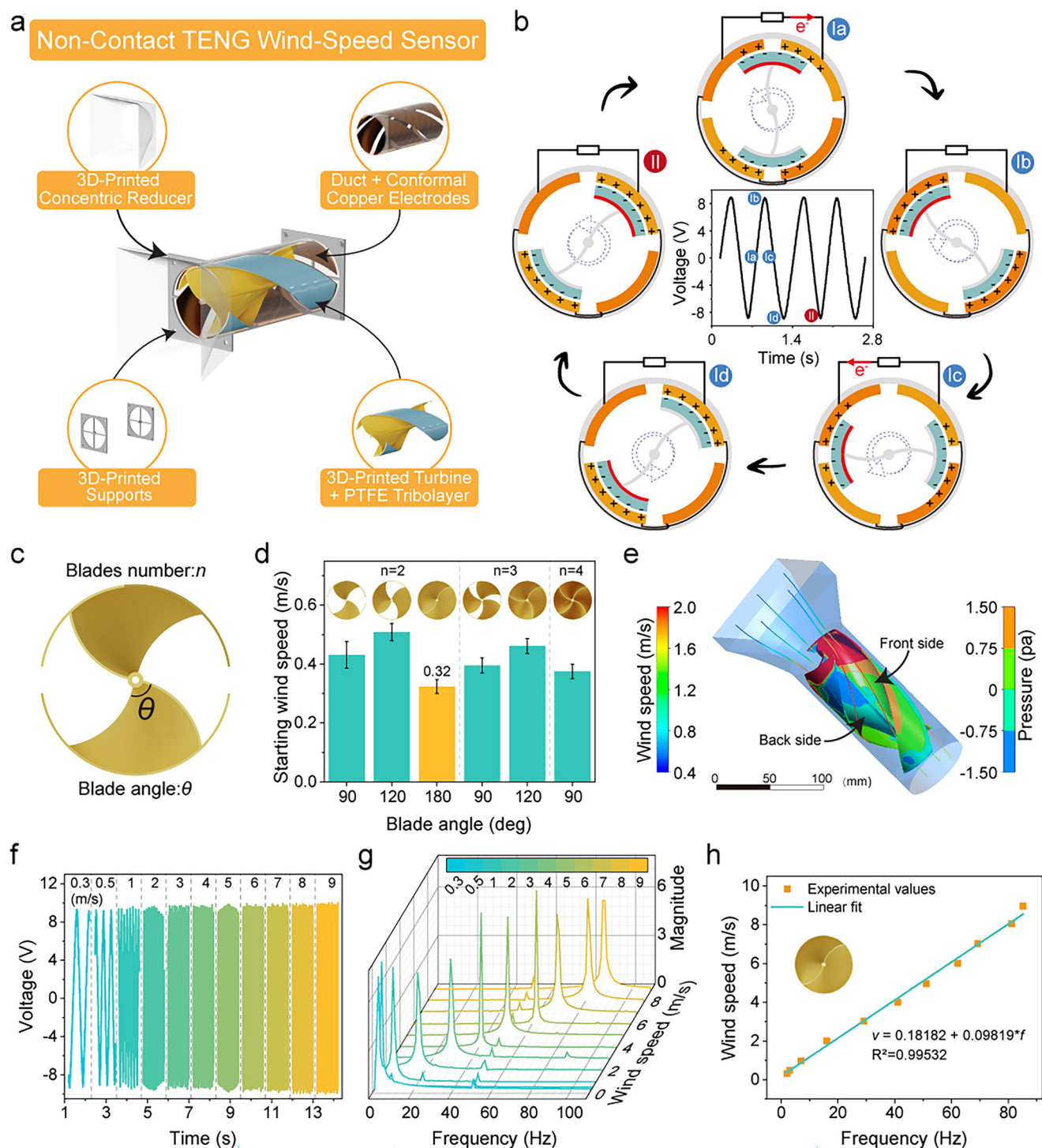


**Fig. 2 | Design, optimization, and calibration of a turbine-based non-contact TENG employed as a wind-speed sensor.** **a** Schematic representation of the structure and various components of the non-contact TENG used as a wind-speed sensor in the TESS. **b** Graphical illustration of the working principle of the non-contact TENG. **c** Schematic diagram of the blade geometry employed in the turbine, along with the influencing parameters. **d** Variation of starting wind speed as a function of the blade number, with  $n = 2, 3, 4$ , and blade angles for  $\theta = \{90^\circ, 120^\circ, 180^\circ\}$ . **e** Results from ANSYS simulations depicting the pressure

difference between the two faces of a blade in the non-contact TENG as airflow occurs through the reducer and duct, at an initial wind speed of  $0.5 \text{ m s}^{-1}$ . **f** Voltage signal produced by the non-contact TENG wind-speed sensor as wind speed increases from  $0.3$  to  $9 \text{ m s}^{-1}$ . **g** Frequency distribution obtained by the Fast Fourier Transform of the signal produced by the non-contact TENG at varying wind speeds. **h** Relationship between the frequency of the non-contact TENG's output signal and the surrounding wind speed.

At an environmental wind speed of  $0.5 \text{ m s}^{-1}$ , the airflow passing through the reducer hits the turbine at a speed over  $2 \text{ m s}^{-1}$ , owing to the Bernoulli effect (colored streamlines in Fig. 2e). Under these conditions, the unique arc shape of this turbine's blade facilitates a

considerable pressure differential ( $\Delta P \hat{=} 3 \text{ Pa}$ ) between the front and back surfaces of the blades, that initiating rotation. In contrast, the other turbine configurations exhibit less favorable performance under the same wind speed conditions (Supplementary Fig. 5).

To measure the ambient wind speed using our non-contact TENG, we focused on the frequency of the generated signal rather than its amplitude, which exhibited only minor variations (Fig. 2f). Using a Fast Fourier Transform (FFT) to the raw signal, we extracted its frequency (Fig. 2g). Upon plotting the wind speed as a function of the frequency of the non-contact TENG, we observed a linear relationship between these two parameters (Fig. 2h). The excellent linearity of this relationship, spanning a wind speed range from 0.32 to 8.97 m s<sup>-1</sup>, is demonstrated by an R-squared coefficient of 0.99532, highlighting the potential efficacy of this self-powered device for the targeted application.

### A Mixed-Mode TENG to harvest wind energy

To supply the necessary power for acquiring, compiling, and transmitting signals from the TENG wind-speed sensor and the other sensors in the TESS's node, we designed a Mixed-Mode TENG power generator, as depicted in Fig. 3a. This TENG incorporates a rectangular reducer to accelerate airflow through Bernoulli effect, while a spoiler generates vortex-induced vibrations (VIV) that provokes the oscillation of the FEP film fixed at the center of the spoiler. This film serves as the triboelectric layer, which impacts the copper electrodes on either side of the rectangular air duct, thus generating electrical power via contact electrification and electrostatic induction as the film oscillates (Supplementary Fig. 6). Our design relies on a TENG working mixed-mode that synergistically combines the advantages of both contact-separation and free-standing configurations (Fig. 3b), yielding simultaneously high output and exceptional durability. A more detailed description is provided in Supplementary Note 6. The Mixed-Mode TENG achieves a peak-to-peak output of 4.55 kV, with broadened peaks exhibiting unusual waveforms (Fig. 3c) that will be discussed later. This working mode is achieved by optimizing the spoiler design (Supplementary Table 3) via CFD and selecting suitable materials. Consequently, the air duct generates alternating vortex-induced upward and downward pressures, reaching peak values of about 1.5 Pa (Fig. 3d) and traveling at speeds exceeding 1.2 m s<sup>-1</sup>, even when the wind speed at the duct inlet is merely 0.5 m s<sup>-1</sup> (Supplementary Fig. 7). This oscillating pressure wave initiates the motion of the FEP tribolayer (Fig. 3e) and forces it to alternatively and simultaneously contact the upper and lower electrodes in both the upstream and downstream sections of the TENG (Fig. 3f, I and IV). High-frame-rate video analyses have verified the successful realization of the proposed working principle (Supplementary Video 1), which facilitates a comprehensive analysis of the electro-mechanical coupling process in the Mixed-Mode TENG (Fig. 3, c, f). This analysis is particularly relevant here, considering the unusual waveform of the output signal.

Indeed, the high-speed camera images reveal the six expected states of the Mixed-Mode TENG during a complete motion cycle (Supplementary Fig. 8). When the contact areas between the film and the upper and lower electrodes are equal (Fig. 3f, I) under the effect of vortex-induced pressure, the voltage signal is zero (Fig. 3c, I). As the film is rapidly pushed downward by vortex-induced pressure and gravity, the contact area with the bottom electrode increases quickly until full contact is achieved (Fig. 3f, II). At this moment, the signal quickly reaches its maximal positive value (Fig. 3c, II). The interplay of these two forces leads to the far end of the film to bounce back on the surface of the bottom electrode, generating a shockwave that propagates along the film (Fig. 3f, III). This shockwave is responsible for the waveforms observed in Fig. 3c, III and its inset, and the separation and contact of the film with the electrode leads to signal broadening, which extends the duration of the voltage output. Subsequently, the contact areas of the film with the upper and lower electrodes become equal again (Fig. 3f, IV), and the voltage signal returns to zero (Fig. 3c, IV). The film then contacts the upper electrode and gradually separates from the lower electrode under the action of vortex-induced pressure (Fig. 3f, V), causing the voltage signal to increase in the negative

direction (Fig. 3c, V), eventually reaching its maximum negative value (Fig. 3c, V). It is worth noting that during the upward motion of the film, the vortex-induced pressure needs to overcome gravity. As a result, when the contact area with the upper electrode reaches its maximum, the film still remains in contact with the lower electrode (Fig. 3f, VI), which explains the slower rise of the voltage signal in the negative direction and the asymmetry in the peak-to-peak value. More importantly, we observed that step III (Fig. 3f) is diminished or absent when the TENG is positioned vertically or exposed to strong wind speeds (above 4 m s<sup>-1</sup>), as seen in Supplementary Video 1. The latter is a consequence of the increased frequency in vortex generation at higher wind speeds prevents the film from resting on the bottom electrode and the occurrence of the shockwave observed at Step III (Fig. 3f). As a result, the Mixed-Mode TENG's voltage output decreases (Fig. 3g and Supplementary Fig. 9).

To verify that the TENG operates in a mixed-mode configuration rather than as a simple free-standing TENG, we analyzed its output in correlation with high-speed camera images (see Supplementary Note 7). This analysis revealed that while the output signal generally correlates with the difference in contact area between the film and the two electrodes, deviations from this trend were observed. In a purely free-standing TENG, the output is expected to strongly correlate with the variation in contact area between the two electrodes. To further investigate, we replicated the device using a linear motor to precisely control its motion (see Supplementary Note 8). The results indicate that the TENG's output arises from both the variation in contact area and the changing distance between the film and the two electrodes. These findings confirm that the device operates as a Mixed-Mode TENG.

To achieve the maximum output voltage of the device illustrated in Fig. 3c, we evaluated the Mixed-Mode TENG performance over a range of wind speeds typical for mining environments, approximately 4 m s<sup>-1</sup>. Initially, we tested the performance of the Mixed-Mode TENG using different materials as tribolayers (Fig. 3h), choosing an arbitrary thickness of 100 μm. Among them, fluorinated ethylene propylene (FEP) demonstrated the highest performance, delivering an output voltage of 4.55 kV. PI was excluded from consideration due to its excessively high starting wind speed and poor performance. We also tested thinner films to lower the starting wind speed. However, we found that films with thicknesses less than 100 μm yielded lower power outputs at a fixed wind speed of 4 m s<sup>-1</sup> (Fig. 3i). For all tested materials, we observed a decrease in output beyond a certain wind speed value, indicating that the operational mechanism of the Mixed-Mode TENG described above is likely applicable across different materials (Supplementary Fig. 10).

### Optimization of power management systems and tests

Although the Mixed-Mode TENG generates a remarkable alternating current (AC) output voltage of 4.55 kV peak-to-peak, such high-voltage, low-current AC power cannot directly drive a circuit board. Moreover, the inherently high-entropy nature of wind energy results in long-term fluctuations in the TENG output, which can lead to unstable operational performance. To address these issues, we employed a self-driven power management system (PMS) to convert and stabilize the output signal. Compared to full-bridge rectifiers, a PMS offers the dual advantage of not only rectifying the current but also controlling the storage and release logic of the energy harvested by the Mixed-Mode TENG. This capability enhances both energy harvesting and conversion efficiency, particularly when it is tailored specifically for a given TENG. Additionally, since our goal is for the Mixed-Mode TENG to power an array of gas sensors and a LoRa transmitter, using a PMS capable of delivering a stable output is essential for maintaining signal quality.

In the present work, we designed a PMS which consists of five components (see Fig. 4a): a group of power input ports connected to four Mixed-Mode TENG power generators (Fig. 4a, I), a rectifier circuit

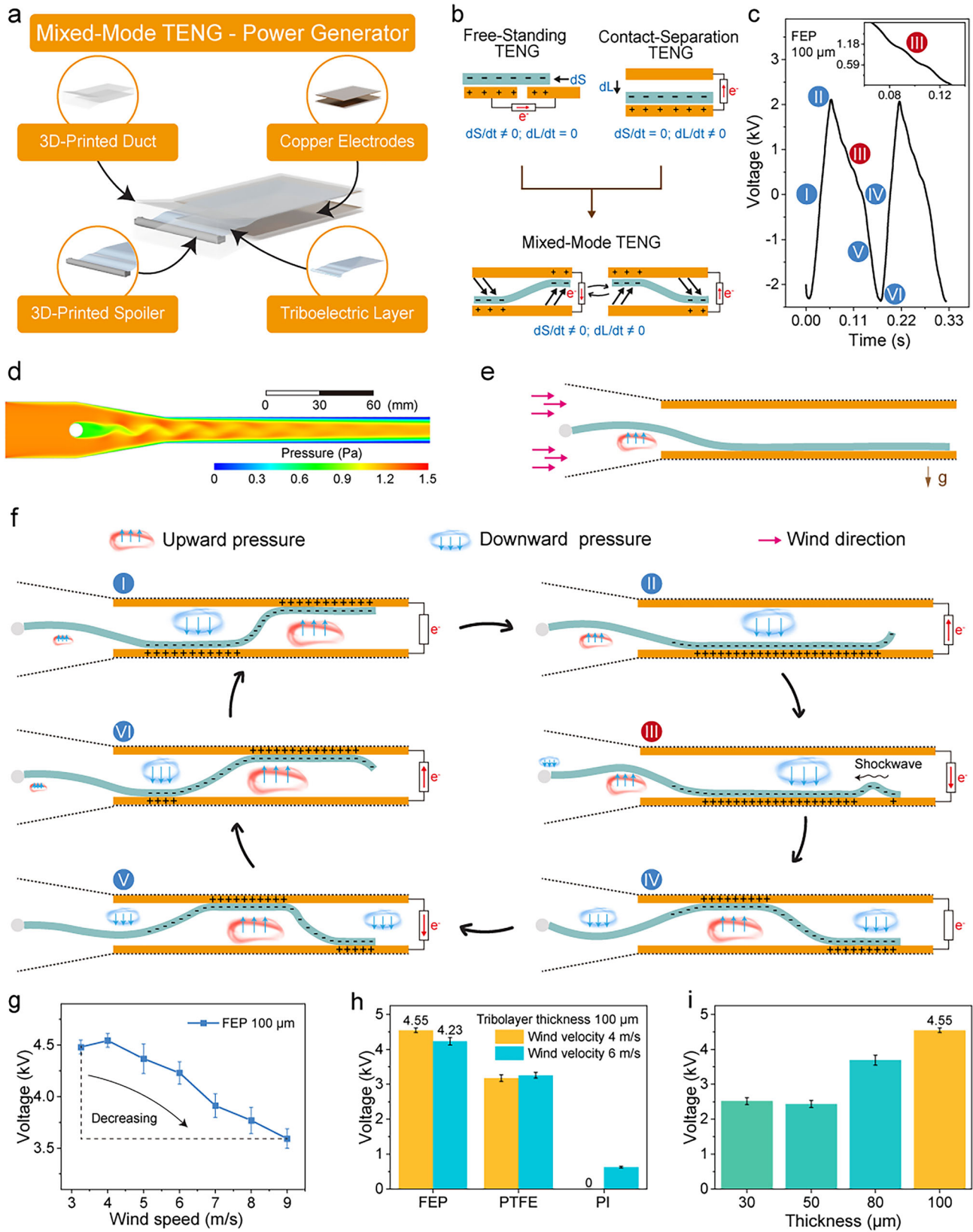


(Fig. 4a, IIa), a buck converter (Fig. 4a, IIb), a link port for energy-storage capacitor (Fig. 4a, III), and a hysteresis control and discharge circuit (Fig. 4a, IV). To elucidate the working principle of this self-driven PMS, we present the circuit diagram in Fig. 4b, accompanied by the voltage waveforms produced by the key components of the circuit. The Mixed-Mode TENG can be modeled with an equivalent circuit

composing an ideal voltage source and a variable capacitor connected in series<sup>18</sup> (see Fig. 4b, I). When the high voltage AC generated by the Mixed-Mode TENG passes through the rectifier circuit, its signal is converted into a high-voltage pulsating direct current (DC) signal (kV) (Fig. 4b, IIa) before reaching the buck converter that decreases the voltage while increases the current characteristics of the signal

**Fig. 3 | Design, characterization, and optimization of a Mixed-Mode TENG for wind energy harvesting.** **a** A schematic illustrating the structure and key components of the Mixed-Mode TENG, used as a wind energy harvester within the TESS. **b** A graphical representation of the free-standing, contact-separation, and Mixed-Mode working modes of TENGs. **c** Voltage signal produced by the Mixed-Mode TENG. **d** Results from an ANSYS simulation demonstrating the oscillating pressure created by the vortex generated in the airflow, induced by the spoiler placed at the reducer inlet. **e** Diagram showing the initial operational stage of the Mixed-Mode

TENG when wind first enters the device. **f** Stepwise depiction of the motion in the horizontally oriented Mixed-Mode TENG, with indicators corresponding to the distinct phases observed in the electrical signal. **g** Peak-to-peak voltage output of the Mixed-Mode TENG as a function of wind speed. **h** Peak-to-peak voltage output for various tribolayers in the Mixed-Mode TENG at wind speeds of 4 and 6 m s<sup>-1</sup>. **i** Peak-to-peak voltage output from the Mixed-Mode TENG equipped with FEP films of varying thickness.

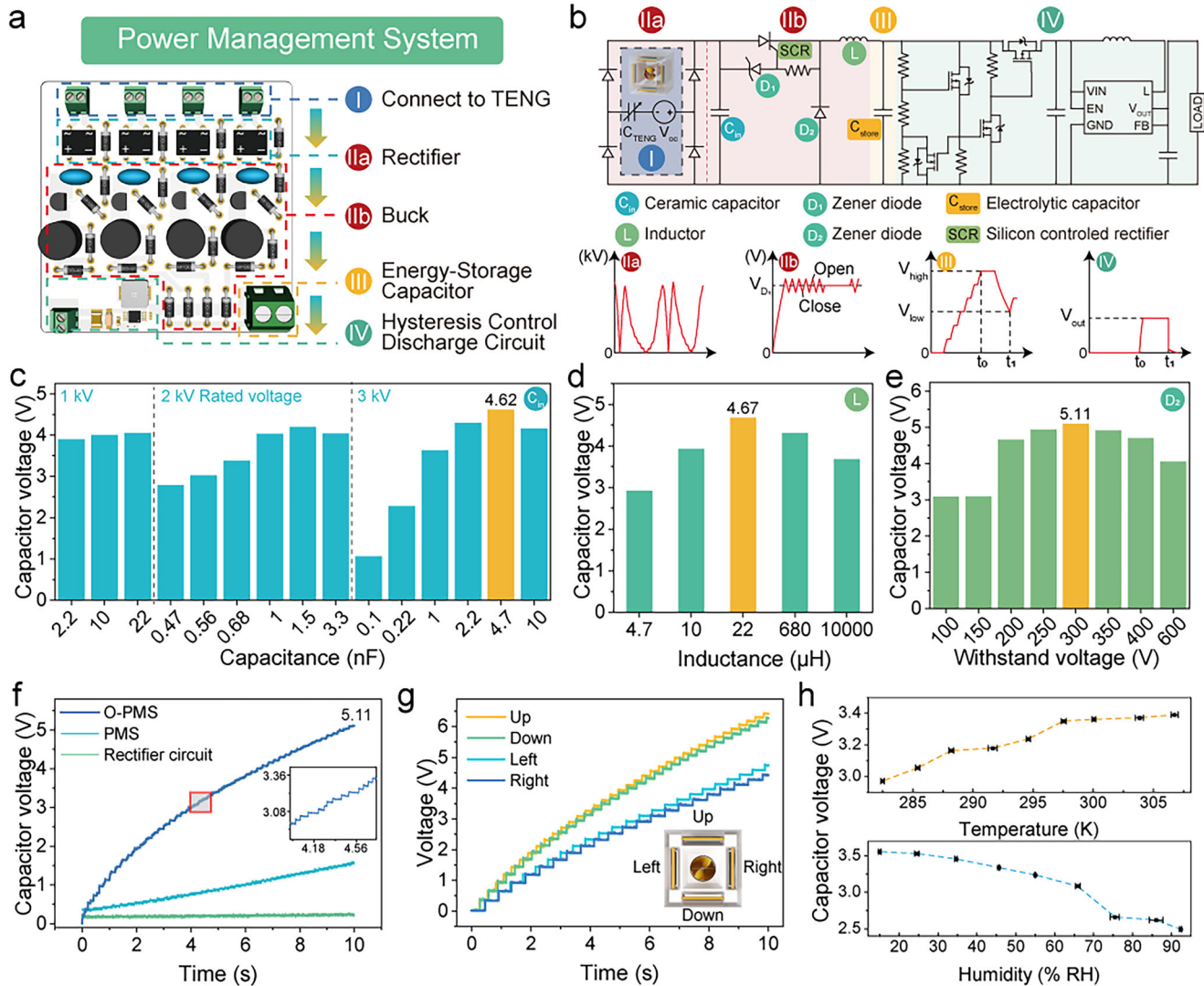


**Fig. 4 | Principles and optimization of a self-driven power management system (PMS) for Mixed-Mode TENGs used as wind energy harvester.** **a** Schematic representation of the general structure of the PMS integrated within the TESS. **b** Circuit diagram illustrating the PMS and its working principles. The voltage stored in the storage capacitor  $C_{store}$  (470  $\mu$ F) by the PMS and Mixed-Mode TENGs working in tandem as a function of (c) the capacitance and rated voltage values of  $C_{in}$ , (d) the inductance value of the inductor  $L$ , and (e) the withstand voltage of the zener diode  $D_2$ . **f** Comparison of the performance of Mixed-Mode TENGs equipped

with a rectifier bridge, a standard PMS, and an optimized PMS (O-PMS) in charging a storage capacitor  $C_{store}$  of 470  $\mu$ F over a period of 10 s. **g** Assessment of the charging efficiency between horizontally and vertically aligned Mixed-Mode TENGs in charging a storage capacitor  $C_{store}$  of 100  $\mu$ F over a period of 10 s. **h** Effect of environmental parameters, specifically temperature (top) and relative humidity (bottom), on the capability of Mixed-Mode TENGs to charge a storage capacitor  $C_{store}$  of 3300  $\mu$ F over a period of 60 s. Data from (c–g) were acquired at a wind speed of 4.05 m s<sup>-1</sup>.

(Fig. 4b, IIb). This transformation of the signal enables the PMS to store energy into capacitors (Fig. 4b, III). The stored energy in the storage capacitor  $C_{store}$  can then be discharged to power simple electronic components and devices, such as LEDs<sup>22</sup> and thermometers<sup>23</sup>. However, the output power fluctuations may lead to situations where the capacitors fully discharge before the sensors complete their measurement cycles, or before the CPU finishes compiling the data, or prior to transmission by the LoRa transmitter. To address this, a

hysteresis circuit is incorporated to discharge the storage capacitor  $C_{store}$  (Fig. 4b, III) when its store voltage reaches a predetermined upper threshold ( $V_{high}$ ), and to cut off power supply to the load circuit when a predetermined lower threshold ( $V_{low}$ ) is reached. The detailed principles of the hysteresis circuit are discussed in Supplementary Note 9. A buck converter placed after the hysteresis control provides a continuous, regulated  $V_{out}$  supply to the load circuit (Fig. 4b, IV). At this stage, as long as airflows through the Mixed-Mode TENG, the

coupled Mixed-Mode TENGs and PMS can deliver a stable DC power to the load circuit during the discharge cycle.

To enhance the energy conversion efficiency of the PMS, we used a Silicon Controlled Rectifier (SCR) circuit to realize a fully passive buck topology with feedforward control (see detailed explanation in Supplementary Note 10). Initially, our focus was on identifying the optimal impedance value for  $C_{in}$ ; excessively high impedance can lead to a mismatch with the Mixed-mode TENG power generator, causing signal reflection and resulting in power losses. The experimental results presented in Fig. 4c demonstrate that a capacitor with a withstand voltage of 3 kV and a capacitance of 4.7 nF enables the Mixed-Mode TENGs and PMS to charge a 470  $\mu$ F capacitor to up to 4.62 V within a period of 10 s (Fig. 4c, in yellow). Subsequently, we optimized the inductance value of the Inductor L. Our findings indicate that utilizing a 22  $\mu$ H inductor allows the Mixed-Mode TENGs and PMS combo to charge the 470  $\mu$ F energy-storage capacitor to 4.67 V within a period of 10 s (Fig. 4d). Finally, we optimized the choice of zener diode used in  $D_2$  (as shown in the buck circuit, Fig. 4b, IIb). We considered that the withstand voltage of the zener diode is inversely proportional to its conduction voltage drop. Among all withstand voltage values tested in  $D_2$ , the results in Fig. 4e illustrate that the optimal performance is achieved with a zener diode rated for a withstand voltage of 300 V.

Based on these findings, we developed a fully optimized self-driven PMS (O-PMS) circuit board and compared its performance with a full-bridge rectifier circuit (without buck topology) and a non-optimized PMS. The results indicate that the O-PMS allows the Mixed-Mode TENGs to charge a 470  $\mu$ F storage capacitor to 5.11 V within 10 s, as shown in Fig. 4f. In contrast, after the same duration, the power supply comprising the Mixed-Mode TENGs and the rectifier bridge or non-optimized PMS charged the 470  $\mu$ F to only 0.24 and 1.55 V, respectively. Compared to a full-bridge rectifier, the non-optimized PMS demonstrated an efficiency improvement of 4071%. However, the difference in conversion efficiency becomes even more striking when comparing these two systems with the O-PMS. The latter exhibits a conversion efficiency that is 45234% higher than that of the full-bridge rectifier and 987% higher than that of the non-optimized PMS (Supplementary Note 11). Furthermore, we evaluated the charging capacity of the capacitors from four Mixed-Mode TENGs positioned differently within the TESS, as illustrated in Fig. 4g. The upper Mixed-Mode TENG successfully charged a 100  $\mu$ F capacitor to 6.42 V within 10 s (at a wind speed of 4.05  $\text{m s}^{-1}$ ), exhibiting a power density of 16.36  $\text{mW m}^{-2}$ . Notably, we observed that the charging efficiency of the Mixed-Mode TENGs arranged horizontally exceeded that of those positioned vertically, which is consistent with the theoretical analysis presented in Fig. 3. Finally, we measured the output of the O-PMS coupled with the four Mixed-Mode TENGs. The data reported in Supplementary Fig. 11 shows that this system can charge different capacitors (100 to 100000  $\mu$ F, including supercapacitor) and maintain a stable output of 3.3 V DC when the voltage of the storage capacitor  $C_{store}$  reaches  $V_{high}$ .

To ensure that the Mixed-Mode TENG/O-PMS power supply can provide enough power under the conditions relevant to our application scenario, we conducted tests across a wide range of temperatures and RH levels (Fig. 4h). At a fixed temperature, we observed that as RH increases, the output from the Mixed-Mode TENG/O-PMS power supply decreases, which aligns with findings from previous reports<sup>24,25</sup> (Fig. 4h, bottom). Conversely, at a fixed RH, we expected that the output would decline with increasing temperature. However, our results revealed a slight increase in energy harvesting efficiency (Fig. 4h, top). This phenomenon has been observed previously in other single-end fixed TENGs<sup>24</sup>. In present case, we attribute the observed increase in energy harvesting efficiency to a reduction in Young's modulus with rising temperature (within the tested temperature range), which facilitates the electro-mechanical coupling<sup>26</sup>.

Meanwhile, these tests demonstrated that, at a RH of 92.3%, the TESS power supply is capable of generating an output sufficient to

charge a 3.3 mF capacitor to more than 2.49 V within 60 s. This result highlights the potential of our system to function effectively in the challenging conditions typically encountered in mining environments.

### Principles and optimization of a low-power wireless sensor node and field-test results

In the preceding sections of this manuscript, we designed a wind-speed sensor based on a non-contact TENG, Mixed-Mode TENGs and an O-PMS for energy harvesting. To effectively acquire and transmit data from the TENG wind-speed sensor, a low-power data acquisition circuit is required, complemented by a low-power transmission circuit. Moreover, as outlined in the introduction, this platform also aims to measure the concentrations of noxious gases (CO, NO<sub>2</sub>, NH<sub>3</sub>). To fulfill these objectives and complete the TESS, a low-power wireless sensor node was designed (Fig. 5a). This platform is equipped with an analog-to-digital converter (ADC) that captures data from the TENG wind-speed sensor after it has undergone processing through a precision operational amplifier, rectification filtering, and a voltage detector and comparator. Thereafter, the data acquired by the ADC is sent to the central processing unit (CPU) for compilation. The gas sensors integrated into this circuit board are commercially available solid electrolyte gas sensor, known for their low power consumption and high stability. The signals from these sensors, along with data from temperature, RH, and pressure sensors, are transmitted to the CPU for further processing, via the IIC communication protocol. The CPU then processes and packages the data before transmitting it through the RF core modulation. For the final sensor node, the operating voltage is set at 3.3 V, with a peak current of about 40 mA and a peak power of around 132 mW. During this period, the wireless sensor node performs data acquisition, compilation, and transmission before entering a low-power mode. The static current in low-power mode is only about 2.4 mA (Supplementary Fig. 12).

The TESS, assembled by mortise and tenon, was tested in an underground mining tunnel, where it was subjected to high temperatures, high humidity, and dust. Detailed descriptions of the experimental setups and test conditions are provided in the Methods section. To ensure the accuracy of the wind-speed data from the TESS, we also installed a commercial hot-wire wind-speed sensor in the tunnel. A voltmeter was connected to the TESS circuit board to record its activity (see Methods). Using a handheld device, we verified that the TESS, including its LoRa transmitter and sensor node, was functioning effectively. A photograph of the device used in this experiment is presented in Fig. 5b. To conduct our tests in the mine while respecting legal time restrictions, we added 10 arrays of Mixed-Mode TENG units, each equipped with their own O-PMS. Under these conditions, at a wind speed of 4.25  $\text{m s}^{-1}$ , the TESS power supply charged a 22 mF the storage capacitor  $C_{store}$  from 3.7 to 5.05 V in 160 s and powered the wireless sensor node twice in a period of 6 s (see Fig. 5c, Supplementary Video 2). To obtain as much wind-speed data as possible within a limited time, we removed the three gas sensors and conducted a quick test using a 10 mF the storage capacitor  $C_{store}$  (Supplementary Fig. 13, Supplementary Video 3). We found that the TESS provided a much more stable wind speed value compared with the commercial hot-wire wind-speed sensor (Fig. 5d). This stability can be attributed to the moment of inertia inherent to the turbine, which is absent in the hot-wire sensors. Thus, the turbine is not affected by minor wind speed fluctuations. This characteristic favors the TESS, making its measurement more conducive to the stable operation of mine ventilation systems (Supplementary Note 12).

Subsequently, we left the TESS and the supplementary Mixed-Mode TENGs to operate continuously in the mine, episodically acquiring data over long periods of time. After one month, the duration of one working cycle of the TESS increased from 64.9 to 74 s, reaching 196 s after three months (see Fig. 5e). This increase in duration of work cycle can be attributed to damages endured by the FEP tribolayer and the copper electrodes placed in the Mixed-Mode

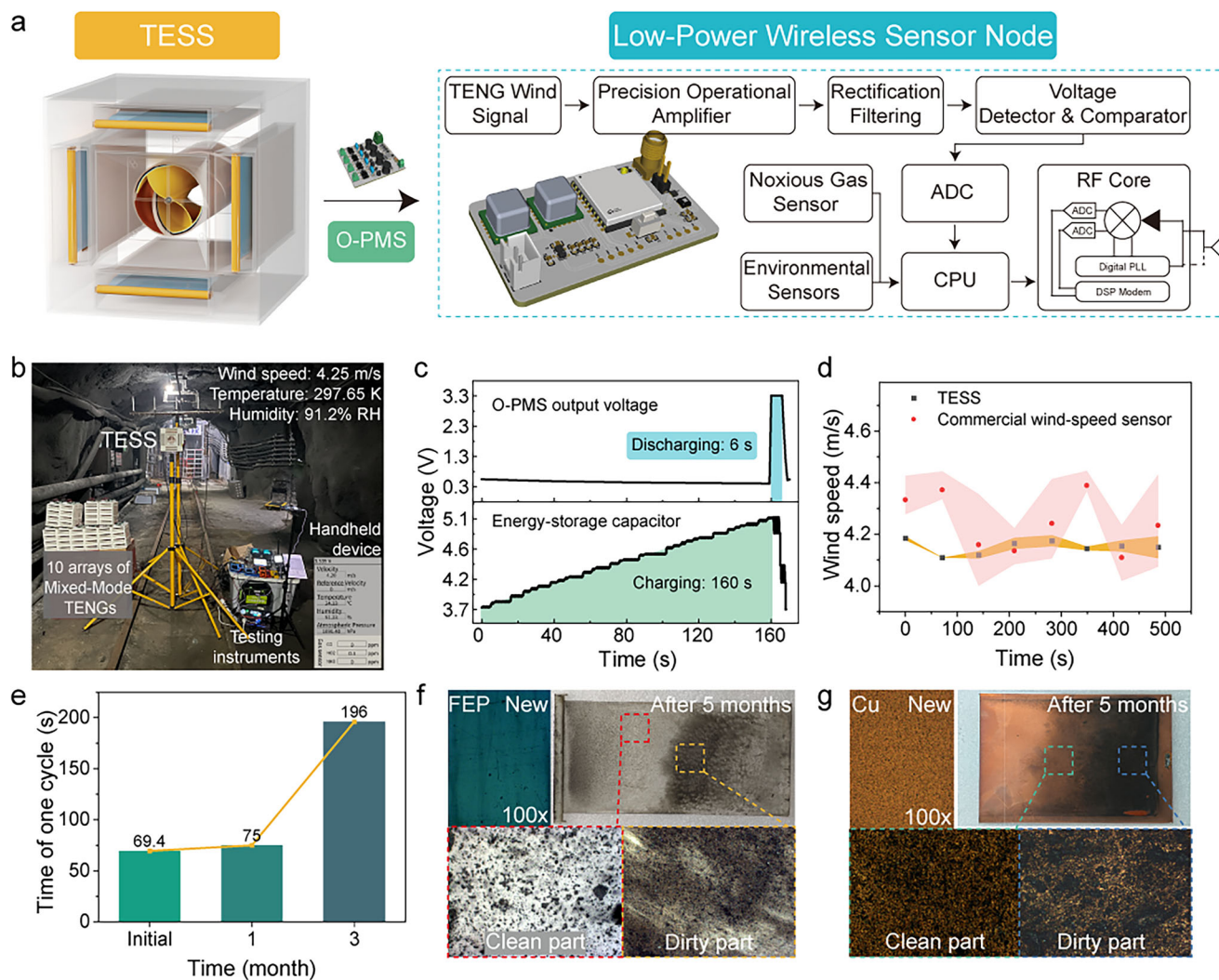


**Fig. 5 | Principles and optimization of a low-power wireless sensor node and field tests of TESS.** **a** Graphical representation of the TESS, highlighting the low-power wireless sensor node and its different parts and functions. **b** Photograph of the on-site experiments, illustrating the TESS along with the environmental parameters and accessories used for data acquisition. **c** Charge/Discharge cycle of the storage capacitor  $C_{\text{store}}$  (22 mF) in the mine for a TESS supplemented by 10 arrays

of Mixed-Mode TENG units, each containing 4 horizontal Mixed-Mode TENGs. **d** Comparison of wind speed values obtained from the TESS using a 10 mF storage capacitor  $C_{\text{store}}$  and a commercial wind-speed sensor. **e** Comparison of the cycle durations, indicating the time interval between each signal, over a period of 3 months. Morphology of the **(f)** FEP tribolayer and **(g)** the copper electrodes of the Mixed-Mode TENGs at the end of the experiment.

TENGs, which resulted from environmental intercalation during operation (See Figs. 5f, g). Under the influence of the heat and centrifugal force, the turbine may encounter the case that it deforms over time until it makes contact with the duct walls, thus stopping rotation. This issue can be likely related to the manufacturing processes and materials chosen for this prototype, specifically the use of a polymer with a low glass transition temperature and low rigidity. In the future, replacing these materials with high-strength alternatives, such as carbon fiber-reinforced polymers, will solve this problem. Finally, after five months of operation in the mine, the Mixed-Mode TENGs and their PMS were brought back to the laboratory for further testing. We found that, after these five months in the mine, the power supply of the TESS could charge a 22 mF capacitor from 3.7 to 5.05 V within 562 s at a wind speed of  $4.39 \text{ m s}^{-1}$  (295.3 K, 85.88% RH) (Supplementary Fig. 14). The system was still able to drive the sensors and transmission node, successfully transmitting data to our handheld device. This is an impressive result, considering the harsh conditions to which the system was exposed for a long period of time, especially given that the TESS operates without requiring power cables connected to the grid or a battery that necessitates more frequent maintenance.

## Discussion

In the present work, a triboelectric self-powered sensing-platform, or TESS, relying on TENGs was designed for measuring wind speed and to supply power to various sensors (CO, NO<sub>2</sub>, NH<sub>3</sub>, temperature, RH, and pressure), and its data acquisition and LoRa transmission modules, through an O-PMS (all within a compact footprint ( $190 \times 190 \times 200 \text{ mm}^3$ ). Its non-contact TENG wind-speed sensor is endowed with a remarkably low starting wind speed of  $0.32 \text{ m s}^{-1}$ , and exhibits excellent linearity across the range from  $0.32$  to  $9 \text{ m s}^{-1}$ , while also providing highly stable measurements.

The TESS employs four Mixed-Mode TENGs that integrate contact-separation (for high durability) and free-standing (for high output) working modes to achieve a peak-to-peak voltage output of 4.55 kV. When combined with an O-PMS, a power density of  $16.36 \text{ mW m}^{-2}$  was achieved. This result surpasses that of previously reported TENGs employing single-end fixed TENG designs. The O-PMS performs the AC-to-DC conversion of the voltage generated by the Mixed-Mode TENGs with an efficiency that is 987% higher than that of a non-optimized PMS and 45234% higher than that of traditional full-bridge rectifiers. The TESS holds considerable advantages over traditional solutions. It is a

completely autonomous, wireless, battery-free and self-powered system capable of delivering a wide variety of information regarding air quality and environmental parameters. Its installation is no longer restricted by tunnel and shaft layouts, allowing for deployment anywhere within the mine at any construction stage. This design reduces the frequency of maintenance and enables quick replacement of damaged electret films and electrodes through the mortise and tenon assembly, further simplifying the maintenance process (Supplementary Video 4).

As such, the present work is a foundational step toward the integration of TENG-based self-powered sensing platforms for intelligent mines and enhancing mine safety monitoring. In a subsequent study, a model for the Mixed-Mode TENG will be established to empower other researchers with predictive tools to conceive power sources for their platforms. Moreover, the TESS and its design principles could benefit other application scenarios where proper ventilation and air quality are critical for guaranteeing the safety of on-site workers, such as underground transit systems, urban utility tunnels, and environmental monitoring in extreme conditions. Furthermore, the development of such self-powered, low-power LoRa-based wireless environmental sensing technologies is expected to positively contribute to the global advancement of sustainable and intelligent sensing infrastructures for industrial safety and environmental monitoring.

## Method

### Fabrication of a wind-speed sensor based on non-contact TENGs and curved-edge turbine

The turbine adopts dimensions of 140 mm in length and 60 mm in diameter, with a central aperture designed to host a tungsten shaft. The two ends of the tungsten steel shaft (150 mm in length and 2 mm in diameter) are supported by ceramic bearings (NSK, Japan) disposed at the center of the 3D-printed cross-shaped supports located at each extremity of the circular air duct (150 mm in length and 64 mm in diameter). A rectangular 3D-printed concentric reducer is integrated at the inlet of the circular air-duct, joint with the air duct by a square-to-circular contraction air inlet, with a square inlet side length of 100 mm. These elements are assembled by a mortise and tenon. The last two elements represent an added 60 mm to the overall assembly, resulting in a total length of 200 mm.

The 3D-printed turbine of the TENG wind-speed sensor features blades with curved edges, which are equipped with winglets at the extremities opposite to the central axis of the turbine. These winglets are designed to carry an adhesive film of PTFE (180  $\mu\text{m}$  in thickness, supplied by Chukoh, Japan) on the surface facing the inner walls of the air duct, serving as the moving electret for the non-contact TENG. Four spiraled copper electrodes (35 mm wide, 150  $\mu\text{m}$  thick, supplied by Dongguan Qingchen Adhesive Products Co., Ltd.) are adhered to the inner wall of the air duct, with a spiral geometry that matches the shape of the turbine's curved-edge blades. These copper electrodes function in pairs, with electrodes facing each other connected by wires to form two groups of positive and negative electrodes.

### Fabrication of a wind-energy harvester based on the Mixed-Mode TENGs

The housing of the Mixed-Mode TENGs comprises two sections that were 3D-printed in a single piece. The rectangular reducer, located upstream of the housing, measures 50 mm in length and features a square inlet that adopts dimensions of 100 mm (width) by 30 mm (height), decreasing to 100 mm by 15 mm at the junction with the air duct. The air duct itself is 150 mm long, with a square cross-section of 100 mm by 15 mm.

A spoiler, with a diameter of 7.5 mm, is fixed at the center of the upstream side of the reducer, serving as an anchor point for the friction film (FEP, PI, or PTFE) which measures 190 mm in length and 90 mm in width. The FEP film (provided by Guangzhou Jufu New

Materials Technology Co., Ltd.), PI film (supplied by Zhongshan Chenxi Technology Co., Ltd.), or PTFE film (provided by Taizhou Daoguan New Materials Co., Ltd.) is symmetrically fixed at the spoiler's center (Supplementary Fig. 15).

To insert the top and bottom copper electrodes into the air duct, grooves measuring 150 mm in length, 1.5 mm in width, and 1 mm in height are laid out along the lateral walls near the roof and ceiling of the air duct. The copper electrodes, measuring 150 mm in length, 100 mm in width, and 10  $\mu\text{m}$  in thickness, are adhered to an acrylic plate (150 mm  $\times$  103 mm  $\times$  1 mm). Once assembled, the electrodes are pushed into the grooves to complete the assembly, resulting in an effective maximum contact area between the copper electrode and the film of 150 mm by 90 mm.

### TESS assembly

The TESS is composed of a non-contact TENG serving as a self-powered wind-speed sensor, along with Mixed-Mode TENGs that function as power generators, an O-PMS, and a low-power wireless sensor node. The structural design of the TESS is achieved through mechanical engineering modeling, and the overall structure and internal components are connected using a mortise and tenon joint system. One wind-speed sensor and four Mixed-Mode TENGs are assembled within the 3D-printed housing case (200  $\times$  190  $\times$  190 mm<sup>3</sup>, resin 9400 A) using this mortise and tenon joints, which is intended to facilitate the maintenance and replacement of the various parts of the TESS.

### Design and construction of a wind tunnel for testing TESS in controlled environment

In this work, wind tunnel tests for the TESS were conducted using an anemometer calibration test device (Supplementary Fig. 16, Jianyan Aikang (Beijing) Technology Co., Ltd.). The dimensions of the wind tunnel are 6.96 m in length, 1.52 m in width, and 2.06 m in height. Airflow enters the tunnel through an inlet equipped with a rectifying orifice plate, forming a uniform and stable flow field in the test section. An axial fan is positioned at the outlet of the wind tunnel, with the wind speed controlled by adjusting the fan's rotational speed using a frequency converter. The first test section measures 600 mm  $\times$  600 mm and operates within a wind speed range of 0.15 to 3 m s<sup>-1</sup>, while the second test section measures 200 mm  $\times$  200 mm with a wind speed range of 3 to 30 m s<sup>-1</sup>. Both test sections are constructed from transparent acrylic, allowing for easy observation of the sensor's operation.

To assess the output performance of the TESS under the high-temperature and high-humidity conditions typical within a mine, we conducted experiments in a sealed environmental chamber (Jianyan Aikang (Beijing) Technology Co., Ltd.) (Supplementary Fig. 17). The dimensions of the test section within the environmental chamber are 4 m in length, 4 m in width, and 2.5 m in height. The air inlet and outlet, each equipped with a rectifying orifice plate, are connected by ducts to either side of the chamber to provide a uniform flow field. The return duct connects to the air conditioning inlet, forming a closed-loop system. The air conditioning unit consists of a heater, a frequency-controlled cabinet fan, a water mist generator (for humidity control), and a refrigeration unit. The temperature is controlled through the combined action of the refrigeration unit and the heater, while humidity is controlled by the water mist generator.

## Performance characterization

### Electrical characterization of TESS in wind tunnels

In this study, various instruments were employed for laboratory measurements. The electrical characterization of the TESS was carried out using an electrometer (Keithley 6514, USA). A measurement circuit based on the Kirchhoff's Voltage Law (KVL) was designed, where the TENG output is applied across two

series-connected resistors ( $R_1 = 999 \text{ M}\Omega$ ,  $R_2 = 1 \text{ M}\Omega$ ). The Keithley 6514 electrometer is used to measure the voltage across  $R_2$ . According to the KVL and Ohm's Law, the output voltage of the TENG is calculated as 1000 times the measured voltage across  $R_2$ . Data was acquired via a data acquisition card (NI USB-6356, National Instruments, USA) and the LabVIEW software platform. Wind speed was monitored with a KANOMAX1560 multi-channel anemometer, while temperature and humidity were monitored by a HMD60. The power consumption of the low-power wireless sensor node was assessed using a DMM7510 (Keithley, USA). High-speed imaging was performed using a FASTCAM Mini AX200 camera, equipped with Nikon lenses (50 mm f/1.4 G and 105 mm f/2.8 G).

### Electrical characterization of TESS in mining tunnels

Many instruments are limited in their use within underground mines due to high temperatures, high humidity levels, and dusty environments. Therefore, the underground experiments were completed using the following instruments. The data logger employed was the KST12A0R (Ningbo Keshun Instrument and Meter Co., Ltd.), with a data input type of 4–20 mA. The following 4–20 mA output sensors were connected to the data logger. The capacitive charging voltage and the working voltage of the low-power wireless sensor node were measured by the QY-W2A (Qiyun IoT Products Technology Center, Lishan District) and ME115 (Shanghai Yiheng Electronics Co., Ltd.). Wind speed was monitored by the JY-GD3 (Beijing Zhongyi Link Control Technology Co., Ltd.). Temperature, humidity, and air pressure were measured with the JFY-4 (Kaiyuan Chuangjie (Beijing) Technology Co., Ltd.). CO and NO<sub>2</sub> concentrations were measured by the AS8807 and AS8806 (Dongguan CEM Instruments Co., Ltd.), respectively. NH<sub>3</sub> concentration was measured with the ADKS-1 EDKORS (Changzhou Siert Electromechanical Equipment Co., Ltd.).

### Field-test conditions

Testing in the mine was conducted in an underground mining site located in Shandong Province, China, from December 14th to 15th, 2023, in a tunnel situated 626 m below the surface (i.e., 496 m below sea level). A suitable test location was selected to minimize worker and vehicle traffic, thereby avoiding large fluctuations in airflow. The TESS was installed at a height of 1.5 m above the ground on a quadrupole, a height chosen to facilitate observations and reduce risk of injuries during the experiments. The sensor node and O-PMS are fixed on the top side of the device. Two voltmeters were connected in parallel to the storage capacitor  $C_{\text{store}}$  and output voltage end of the PMS. The data transmitted by the LoRa transmitter is displayed on a handheld device with a homebrew software. To abide to mine's regulations, tests were conducted for 6 h each day. To minimize the time required for underground testing, ten arrays of Mixed-Mode TENGs were installed 1 meter above the floor of the tunnel, on the left side of the TESS. To verify the accuracy of the data acquired by the TESS, a commercial wind-sensor was installed at the upper part of the TESS. Additionally, at a lower height on the right side of the TESS, we placed a device to measure humidity, temperature, and air pressure, as well as detectors to measure the concentrations of CO, NO<sub>2</sub>, and NH<sub>3</sub>. On December 14, 2023, we measured the operating conditions of the TESS with a 10 mF storage capacitor  $C_{\text{store}}$  (Supplementary Fig. 18). During this measurement, the average temperature in the mine was 296.95 K, RH reached 91.1%, and air pressure was 108.34 kPa, with a wind speed of 5.33 m s<sup>-1</sup>. On December 15, measurements were conducted using storage capacitors  $C_{\text{store}}$  with capacitance values of 10, 22, and 100 mF, respectively (Supplementary Fig. 19). On this day, the wind speed in the mine was recorded at 4.25 m s<sup>-1</sup>, with a temperature of 297.65 K, RH of 91.2%, and an air pressure of 108.36 kPa. Subsequently, the TESS and its supplementary Mixed-Mode TENGs were left in the mine for a

durability test over a period of 5 months, with data acquisition conducted at the end of the 1st and 3rd month.

### Reporting summary

Further information on research design is available in the Nature Portfolio Reporting Summary linked to this article.

### Data availability

The data generated in this study are provided in the Source Data file. Source data are provided with this paper.

### References

- Pintus, P. et al. Integrated non-reciprocal magneto-optics with ultra-high endurance for photonic in-memory computing. *Nat. Photon.* **19**, 54–62 (2025).
- Koo, J. H. et al. A vacuum-deposited polymer dielectric for wafer-scale stretchable electronics. *Nat. Electron.* **6**, 137–145 (2023).
- Zhao, X. et al. Transistors and logic circuits based on metal nanoparticles and ionic gradients. *Nat. Electron.* **4**, 109–115 (2021).
- Coughlin, E. E., Hu, J., Lee, A. & Odom, T. W. Light-Mediated Directed Placement of Different DNA Sequences on Single Gold Nanoparticles. *J. Am. Chem. Soc.* **143**, 3671–3676 (2021).
- Zhang, J. et al. Weakly ionized gold nanoparticles amplify immunoassays for ultrasensitive point-of-care sensors. *Sci. Adv.* **10**, eadn5698 (2024).
- Lee, K. et al. Nanoparticle delivery of Cas9 ribonucleoprotein and donor DNA in vivo induces homology-directed DNA repair. *Nat. Biomed. Eng.* **1**, 889–901 (2017).
- Xia, K. et al. Ultra-stable and highly reactive colloidal gold nanoparticle catalysts protected using multi-dentate metal oxide nanoclusters. *Nat. Commun.* **15**, 851 (2024).
- An, Q. et al. Direct growth of single-chiral-angle tungsten disulfide nanotubes using gold nanoparticle catalysts. *Nat. Mater.* **23**, 347–355 (2024).
- Gold Demand Trends Q2 2024. *World Gold Council* <https://www.gold.org/goldhub/research/gold-demand-trends/gold-demand-trends-q2-2024> (2024).
- Mapeta, T. & Rupprecht, S. M. Study of ventilation and cooling in gold mines in South Africa as a means to improve safety and productivity. In *Proceedings of the 26th International Mining Congress and Exhibition of Turkey (IMCET 2019)*, 101–111 (2019).
- Roy, S., Mishra, D. P., Bhattacharjee, R. M. & Agrawal, H. Heat stress in underground mines and its control measures: a systematic literature review and retrospective analysis. *Min. Metall. Explor.* **39**, 357–383 (2022).
- Zvyagintseva, A. V., Sazonova, S. A. & Kulneva, V. V. Analysis of sources of dust and poisonous gases in the atmosphere formed as a result of explosions at quarries of the mining and integrated works. *IOP Conf. Ser.: Mater. Sci. Eng.* **962**, 042045 (2020).
- Ali, F. et al. Investigation and mapping of toxic fumes produced by detonation of ANFO explosives in underground space. *Propellants, Explos., Pyrotech.* **49**, e202400002 (2024).
- Nie, X., Wei, X., Li, X. & Lu, C. Heat treatment and ventilation optimization in a deep mine. *Adv. Civ. Eng.* **2018**, 1529490 (2018).
- Belle, B. Real-time air velocity monitoring in mines - a quintessential design parameter for managing major mine health and safety hazards. *Resour. Oper. Conf.* 184–198 (2013).
- Entwistle, J. A., Hursthouse, A. S., Marinho Reis, P. A. & Stewart, A. G. Metalliferous mine dust: human health impacts and the potential determinants of disease in mining communities. *Curr. Pollut. Rep.* **5**, 67–83 (2019).
- Gren, L. et al. Underground emissions and miners' personal exposure to diesel and renewable diesel exhaust in a Swedish iron ore mine. *Int. Arch. Occup. Environ. Health* **95**, 1369–1388 (2022).

18. Niu, S. & Wang, Z. L. Theoretical systems of triboelectric nanogenerators. *Nano Energy* **14**, 161–192 (2015).
19. Cheng, T., Shao, J. & Wang, Z. L. Triboelectric nanogenerators. *Nat. Rev. Methods Prim.* **3**, 1–13 (2023).
20. Choi, D. et al. Recent advances in triboelectric nanogenerators: from technological progress to commercial applications. *ACS Nano* **17**, 11087–11219 (2023).
21. Jin, D. W. et al. Peeling-induced interfacial roughness and charging for enhanced triboelectric power generation. *Nano Trends* **8**, 100055 (2024).
22. Yang, Y. et al. Triboelectric nanogenerator for harvesting wind energy and as self-powered wind vector sensor system. *ACS Nano* **7**, 9461–9468 (2013).
23. Wang, Y. et al. Multi-functional wind barrier based on triboelectric nanogenerator for power generation, self-powered wind speed sensing and highly efficient windshield. *Nano Energy* **73**, 104736 (2020).
24. Zhao, Z. et al. Freestanding flag-type triboelectric nanogenerator for harvesting high-altitude wind energy from arbitrary directions. *ACS Nano* **10**, 1780–1787 (2016).
25. Nguyen, V. & Yang, R. Effect of humidity and pressure on the triboelectric nanogenerator. *Nano Energy* **2**, 604–608 (2013).
26. Rae, P. J. & Brown, E. N. The properties of poly(tetrafluoroethylene) (PTFE) in tension. *Polymer* **46**, 8128–8140 (2005).
27. Wang, P. et al. An ultra-low-friction triboelectric–electromagnetic hybrid nanogenerator for rotation energy harvesting and self-powered wind speed sensor. *ACS Nano* **12**, 9433–9440 (2018).
28. Li, X. et al. Breeze-driven triboelectric nanogenerator for wind energy harvesting and application in smart agriculture. *Appl. Energy* **306**, 117977 (2022).
29. Su, E. et al. Rationally designed anti-glare panel arrays as highway wind energy harvester. *Adv. Funct. Mater.* **33**, 2214934 (2023).
30. Rahman, M. T. et al. Natural wind-driven ultra-compact and highly efficient hybridized nanogenerator for self-sustained wireless environmental monitoring system. *Nano Energy* **57**, 256–268 (2019).
31. Wang, J. et al. Self-powered wind sensor system for detecting wind speed and direction based on a triboelectric nanogenerator. *ACS Nano* **12**, 3954–3963 (2018).
32. Fu, X. et al. Breeze-wind-energy-powered autonomous wireless anemometer based on rolling contact-electrification. *ACS Energy Lett.* **6**, 2343–2350 (2021).
33. Zhang, Y. et al. An Ultra-durable windmill-like hybrid nanogenerator for steady and efficient harvesting of low-speed wind energy. *Nano-Micro Lett.* **12**, 175 (2020).
34. Guo, Y. et al. Harvesting wind energy: A hybridized design of pin-wheel by coupling triboelectrification and electromagnetic induction effects. *Nano Energy* **60**, 641–648 (2019).
35. Li, G. et al. Triboelectric-Electromagnetic Hybrid Wind-Energy Harvester with a Low Startup Wind Speed in Urban Self-Powered Sensing. *Micromachines* **14**, 298 (2023).
36. Lin, H. et al. Angle-shaped triboelectric nanogenerator for harvesting environmental wind energy. *Nano Energy* **56**, 269–276 (2019).
37. Wang, Y. et al. A novel humidity resisting and wind direction adapting flag-type triboelectric nanogenerator for wind energy harvesting and speed sensing. *Nano Energy* **78**, 105279 (2020).
38. Chen, X. et al. A Triboelectric nanogenerator exploiting the bernoulli effect for scavenging wind energy. *Cell Rep. Phys. Sci.* **1**, 100207 (2020).
39. Liu, D. et al. Wind-driven self-powered wireless environmental sensors for Internet of Things at long distance. *Nano Energy* **73**, 104819 (2020).
40. Yuan, S. et al. Scavenging breeze wind energy (1–8.1 m s<sup>-1</sup>) by minimalist triboelectric nanogenerator based on the wake galloping phenomenon. *Nano Energy* **100**, 107465 (2022).
41. Sun, W., Ding, Z., Qin, Z., Chu, F. & Han, Q. Wind energy harvesting based on fluttering double-flag type triboelectric nanogenerators. *Nano Energy* **70**, 104526 (2020).
42. Tcho, I.-W. et al. A flutter-driven triboelectric nanogenerator for harvesting energy of gentle breezes with a rear-fixed fluttering film. *Nano Energy* **98**, 107197 (2022).
43. Son, J. et al. Ultrahigh performance, serially stackable, breeze driven triboelectric generator via ambient air ionizing channel. *Adv. Mater.* **35**, 2300283 (2023).
44. Liu, D. et al. Sustainable long-term and wide-area environment monitoring network based on distributed self-powered wireless sensing nodes. *Adv. Energy Mater.* **13**, 2202691 (2023).

## Acknowledgements

This research was supported by the National Natural Science Foundation of China (5240040361, 52192610 and 52192613), the Beijing Natural Science Foundation (L247036), and the National Key R & D Project from Minister of Science and Technology (2021YFA1201601). We warmly thank the mine workers Guojian Jiang, Tao Yu and Yuchao Lu who helped us conducting our field experiments and ensured our safety during our stay. We thank Zhao Gao, Menghui Xiao and Haixing Li for helping assemble the devices.

## Author contributions

L.L., X.L., C.D. and L.Z. conceptualized the experiments and methodology design. L.L. fabricated the TESS and collected the test data. L.L. and Y.S. designed the algorithm and processed the collected sensing data. Y.S. and L.L. assisted with designing and fabricating the circuit. Y.S. and L.L. designed the interface programme for data acquisition and visualization. L.L. and L.Y.L. contributed to the characterization of the materials and devices. L.L., A.B., Y.W., X.L., L.Y.L., X.X.L. and B.Y. assisted with the fabrication of the sensor-array. L.L., A.B. and L.Z. assisted in designing the figures. M.W., A.B., and L.L. developed the theoretical model. L.L., J.C. and B.Y. contributed to the development of the test equipment. L.L., Y.S., A.B. and L.Z. contributed to discussions about the paper. Y.W., C.D., L.Z. and Z.L.W. provided financial support and oversight of the whole project. L.L., Y.S. and A.B. wrote the paper. All authors participated in manuscript revision and refinement.

## Competing interests

L.L., Y.W., C.D., and L.Z. are inventors on CN patent (No. 202410463939.5) submitted by the University of Science and Technology Beijing that covers the structure of the TESS and the wind-speed monitoring method described in this paper. The remaining authors declare no competing interests.

## Additional information

**Supplementary information** The online version contains supplementary material available at <https://doi.org/10.1038/s41467-025-60418-9>.

**Correspondence** and requests for materials should be addressed to Yuan Wang, Cuifeng Du, Zhong Lin Wang or Laipan Zhu.

**Peer review information** *Nature Communications* thanks the anonymous reviewers for their contribution to the peer review of this work. A peer review file is available.

**Reprints and permissions information** is available at <http://www.nature.com/reprints>

**Publisher's note** Springer Nature remains neutral with regard to jurisdictional claims in published maps and institutional affiliations.

**Open Access** This article is licensed under a Creative Commons Attribution-NonCommercial-NoDerivatives 4.0 International License, which permits any non-commercial use, sharing, distribution and reproduction in any medium or format, as long as you give appropriate credit to the original author(s) and the source, provide a link to the Creative Commons licence, and indicate if you modified the licensed material. You do not have permission under this licence to share adapted material derived from this article or parts of it. The images or other third party material in this article are included in the article's Creative Commons licence, unless indicated otherwise in a credit line to the material. If material is not included in the article's Creative Commons licence and your intended use is not permitted by statutory regulation or exceeds the permitted use, you will need to obtain permission directly from the copyright holder. To view a copy of this licence, visit <http://creativecommons.org/licenses/by-nc-nd/4.0/>.

© The Author(s) 2025